

Numerical investigation of aeroelastic and three dimensional effects for an airfoil in transonic flow

S. Surrey*, A.D. Gardner†, H. Mai‡ and C. Klein§

Abstract

Numerical investigations on an OA209 airfoil with flow control by air jets are compared with experiments at static conditions. RANS calculations for the DNW-TWG wind tunnel with a 1 m x 1 m adaptive-wall test section setup are performed to investigate the three-dimensional effects of this nominally two-dimensional configuration. Aeroelastic investigations of the midspan displacement, by coupling with a finite-element model of the airfoil at $Ma = 0.4$ and $Re = 2.8 \cdot 10^6$ are in good agreement with deformation measurements by stereography. A small influence of the airfoil deformation on the aerodynamics can be seen in the numerical results, but the effect is less than the experimental uncertainty. A numerical investigation of flow control by air jets at the leading edge is presented for multiple static test cases at $Ma = 0.3$ and $Re = 1.16 \cdot 10^6$. A variation of air jet pressure and its influence on stall suppression is shown to be in good agreement with experiments except in the case where no flow control is used (blowing pressure of zero). Surface pressure distributions are shown to be in good agreement with experimental pressure distributions from pressure sensitive paint.

Nomenclature

A^*	Effective patch surface (m^2)
b	Airfoil model breadth (=997 mm)
c	Airfoil chord (=300 mm)
C_L	Lift coefficient
C_P	Pressure coefficient
d	Airfoil thickness (mm)
f_a	Aerodynamic forces
f_s	Structural forces
h	Deformation (m)
H	Interpolation matrix
K	Efficiency factor
\dot{m}	Mass flow rate through air-jets (kg/s)
Ma	Mach number
p_0	Total pressure at patch surface (Pa)
P_{jet}	Air jet pressure (bar)

*Corresponding Author. German Aerospace Center (DLR), Institute of Aeroelasticity, Bunsenstrasse 10, 37073 Göttingen, Germany. stefan.surrey@dlr.de

†DLR Institute of Aerodynamics and Flow Technology

‡DLR Institute of Aeroelasticity

§DLR Institute of Aerodynamics and Flow Technology

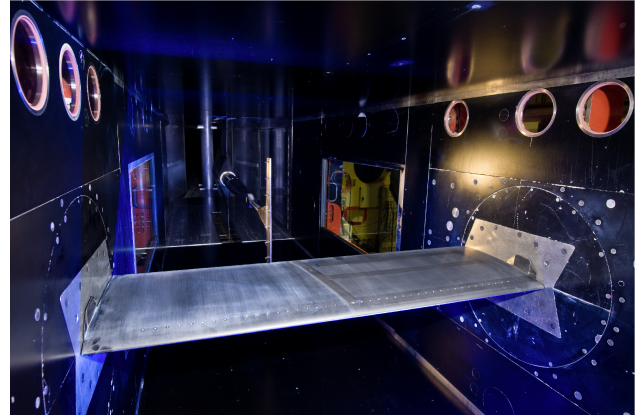


Figure 1: OA209-FCD airfoil installed in the DNW-TWG wind tunnel [1].

q	Generalized displacements
R	Ideal gas constant
Re	Reynolds number
T_0	Total temperature at patch surface (T)
u_s	Phy. deformation of the FE surface (m)
u_a	Phy. deformation of the CFD surface (m)
α	Angle of attack [$^\circ$]
ϕ_a	Interpolated aerodynamic mode shapes
ϕ_s	Structural mode shapes
Ω	Modal stiffness matrix

Introduction

Dynamic flow separation is a well known phenomenon for helicopters in fast forward flight or highly loaded maneuvering flight, resulting a lift overshoot and a pitching moment peak which causes high pitch link loads on helicopters. The DLR has pursued dynamic stall control by Fluidic Control Devices (FCDs) by using high pressure blowing from vertical portholes located at $x/c=0.10$ [1]. This arrangement was tested on a pitching airfoil model in the German-Dutch Wind Tunnel Association's Transonic Wind Tunnel Göttingen (DNW-TWG), as shown in Fig. 1. A reduction of the forces experienced during dynamic stall by 50%-100% was achieved, depending on the test condition.

A number of authors have found a correlation between the control of static stall and the control of dynamic stall. Gardner et al. [2] investigated the air jet blowing of

the configuration investigated in this paper by numerical simulations, showing that configurations which delayed static stall or increased lift for separated flow at static angle of attack also showed good control of dynamic stall. Results by Packard *et al.* with constant blowing through similar jets on a laminar NACA 64₃-618 airfoil [3] showed good control of static laminar separation near the trailing edge of the thick airfoil, with maximum C_{μ} approximately 0.005. Similarly, Prince *et al.* [4] showed control of static stall by a passive air-jet system with vertical portholes on the airfoil suction side.

Singh *et al.* [5] used blowing from angled jets at $M=0.13$ and $Re=1.1 \cdot 10^6$ to control static stall. The jets were located at $x/c=0.12$ and spaced at $y/c=0.1$ along the span with the jet exit pitched at $\phi=30^\circ$ and skewed at $\psi=60^\circ$. Further experiments by the same group [6] on a pitching airfoil found that for constant blowing at $C_{\mu}=0.008$ there was good control of dynamic stall. Mai *et al.* [7] and Heine *et al.* [8] investigated the control of stall on pitching and static airfoils using vortex generators, finding that configurations which controlled dynamic stall also increased lift in the stalled flow, but without delaying the dynamic stall. Rehman and Kontis [9] showed that synthetic jets could control dynamic stall and increase the lift after static stall, while the stall angle was slightly delayed.

Richter *et al.* [10] performed Unsteady Reynolds-averages Navier-Stokes (URANS) calculations to simulate the two-dimensional (2D) flow of a pitching airfoil in the DNW-TWG under dynamic stall conditions. Three-dimensional (3D) effects of pitching airfoils at the DNW-TWG were considered by Klein *et al.* [11]. Klein investigated the 3D effects in the DNW-TWG during dynamic stall and compared the results to 2D calculations. These results showed discrepancies between computations and experiments, which could not be fully explained. The influence of the interaction of aerodynamic forces and airfoil deformation and its effect on the airfoil aerodynamics is discussed in this paper. Different angle of attack of static configurations were investigated by Stickan *et al.* [12] and Mai *et al.* [13] using steady wind tunnel investigations to validate the CFD-FEM-software TAU-PyCSM. Further aeroelastic investigations in a wind tunnel were investigated by Hassan *et al.* [14] for an transport aircraft typical wing.

The 3D flow effects of the OA209 airfoil in transonic flow is investigated in this paper by Reynolds-averaged Navier-Stokes (RANS) computations at static angle of attack. The wind tunnel model includes jet actuators at the leading edge and the presented investigations include a numerical setup to simulate this flow control system. Multiple attached and separated flow conditions at $Ma = 0.3, Re = 1.16 \cdot 10^6$ were performed and compared to experimental results. The influence of air jet pressure was investigated and an estimation to stall control was made. The 3D flow around the portholes was compared to PSP results, to explain and understand the flow control system used.

Numerical methods and simulation setup

The numerical investigations in this paper are performed by the computational fluid dynamic (CFD) solver DLR-TAU and the DLR in-house coupling environment PyCSM. All steady Reynolds-averaged Navier-Stokes (RANS) computations are based on the DLR solver TAU [15]. The CFD solver DLR-TAU is a node-based finite-volume solver which is based on the dual grid approach. During preprocessing a dual grid is created so that the solver is independent of the original grid cell types. The inviscid fluxes were discretized using a second order upwind scheme. All DLR-TAU computations were fully turbulent using a two-equation Menter SST turbulence model. [16] The aeroelastic simulations and the wall adaptation was applied by the DLR-TAU deformation tool which is based on radial basis functions. All numerical grids were created by the unstructured grid generator CentaurTM.

The influence of aeroelastic deformation on the aerodynamics around an airfoil for steady wind tunnel configurations was investigated. The coupling of aerodynamics (Computational fluid dynamics, CFD) and structural dynamics (Finite element method, FEM) is conducted by a weak coupling strategy. The flow solver and the structural solver operate separately in this method. The differences in surface discretization between CFD and FEM need an interpolation method based on scattered data [17]. For each steady aeroelastic simulation presented in this paper, the in-house tool PyCSM was used. PyCSM uses a modal approach with the generalized displacements in vector q , the structural forces f_s and the modal matrix ϕ_s . An equation of $f_s = H^T f_a$ can be defined via an interpolation matrix H based on scattered data interpolation between the aerodynamic and structural surfaces [17]. With these definitions the linear elastic equation can be written as: [18]

$$q = \Omega^{-1} \phi_s^T f_s \quad (1)$$

$$= \Omega^{-1} (H \phi_s)^T f_a \quad (2)$$

$$= \Omega^{-1} \phi_a^T f_a \quad (3)$$

In equation 3 the vector f_a represents the aerodynamic forces on the aerodynamic surface and calculated by CFD simulations. The modal stiffness matrix $\Omega = \text{diag}(\omega_1^2, \dots, \omega_n^2)$ contains the eigenvalues of the structure. The structural mode shapes are represented by ϕ_s and ϕ_a contains the interpolated mode shapes on the aerodynamic surface. In vector q are the generalized displacements. The mode shapes ϕ_s need to be calculated by ANSYSTM. The physical displacements of the aerodynamic surface u_a can be determined by $u_a = \phi_a q$. The structural modes need to be interpolated on the aerodynamic mesh only once during a preprocessing step.

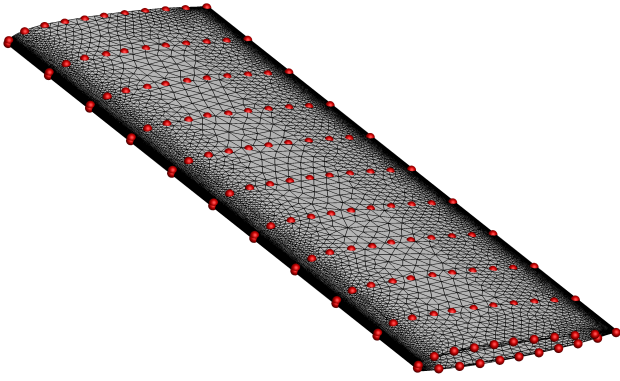


Figure 2: Surface coupling points of the CFD and the FEM grid

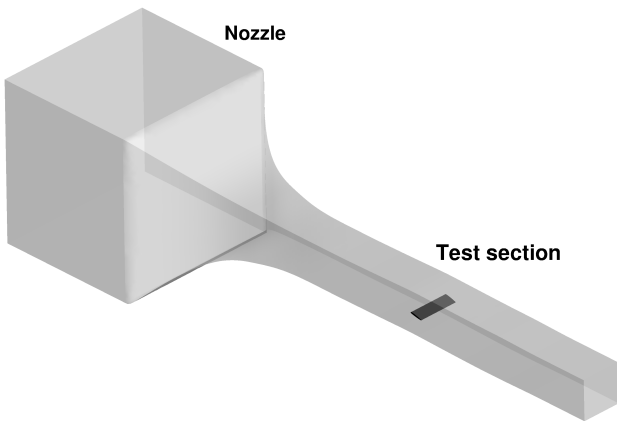


Figure 3: Numerical wind tunnel setup of the DNW-TWG wind tunnel and airfoil model.

The interpolation of the forces to the structure and of the deformation to the CFD grid needs a spatial coupling, which is defined using radial basis functions, enabling the creation of the coupling matrix H . Figure 2 shows the extracted surface nodes of the CFD grid and coupling points of the structural model.

All numerical investigations were made with the complete 1 m x 1 m adaptive-wall test section and nozzle of the DNW-TWG, shown in Figure 3. The computational domain started at the screens and progressed through the 16:1 contraction of the nozzle. The wind tunnel model was an airfoil of OA209 section, mounted 2.2 m downstream of the end of the nozzle, and for the computations the airfoil spanned the entire width of the tunnel, joining the sidewalls with a gapless connection. The computation domain extended a further 4 m downstream to the outflow.

In the experiment the airfoil was constructed of carbon fiber shells around an aluminum spar and instrumented with Kulite pressure transducers on the model midline [1]. The airfoil had a chord length $c=300$ mm and a span $b=997$ mm, with a relative thickness $d/c=0.09$. In contrast to the computations, the experimental setup includes a 1.5 mm gap between the wind tunnel walls and

the airfoil, and this difference is expected to have a local effect on the corner flow in the connection between the airfoil and the wind tunnel wall, but not on the flow at the model midline [19]. The positions of the adaptive top and bottom walls in the simulations were taken from the experiment, where the flexible walls were adjusted to the pressure field of the model to minimize interference effects.

The numerical grid of the aeroelastic simulations had about 9.4 million points and the airfoil had a maximum cell size of 3% chord on the surface and 42 prismatic layers to resolve the boundary layer (Table 1). The wind tunnel model included jet actuators, consisting of a line of 3mm diameter porthole jets at $x/c = 0.10$ with spacing $y/c = 0.067$, and the jet pressure could be varied up to 10bar [1]. The CFD grid of the steady air jet blowing simulations had about 6.2 million nodes, however the grid for the wind tunnel and stagnation chamber was made coarser during a grid optimization step and the airfoil surface points were increased from 35000 for the elastic computations to 150000 for the air blowing simulations. For the steady air jet blowing simulations the maximum surface cell size is 4% chord and the injector cell size is 0.07% chord, with clustering of volume cells around the jets and 38 prismatic layers to resolve the boundary layer. Figure 4 shows the mesh configuration of the air jet simulations.

Table 1: Comparison of the mesh resolutions of the two configurations

Option	Air jet blowing	Aeroelastic
Grid nodes (Million)	6.2	9.4
Prismatic grid		
layers	38	42
y^+	≤ 1	≤ 1
Surface grid		
max. cell size	4%	3%
leading edge cell size	0.12% c	0.1% c
trailing edge cell size	0.2% c	0.2% c
injector cell size	0.07% c	-
Volume grid		
cell size in source near jets	0.6% c	-
cell size in source near airfoil	6.2% c	3.5% c

The aeroelastic simulations were started with a converged simulation of the rigid airfoil. During coupled simulations the loop included 8000 time steps before the aerodynamic forces were interpolated to the structure. All simulations reached the defined convergence criteria (difference in the deformation h_{max} from one iteration to the next was less than 10^{-5} m) after 5 coupling iterations. CFD calculations with and without air jets of the rigid airfoil needed at least 200000 time steps until a converged solution and the defined flow conditions were reached. The flow condition in the wind tunnel setup was iterated by an adjustment of the outlet pressure of the wind tunnel.

The porthole jets were modeled as surface patches with total conditions (pressure, density, temperature) de-

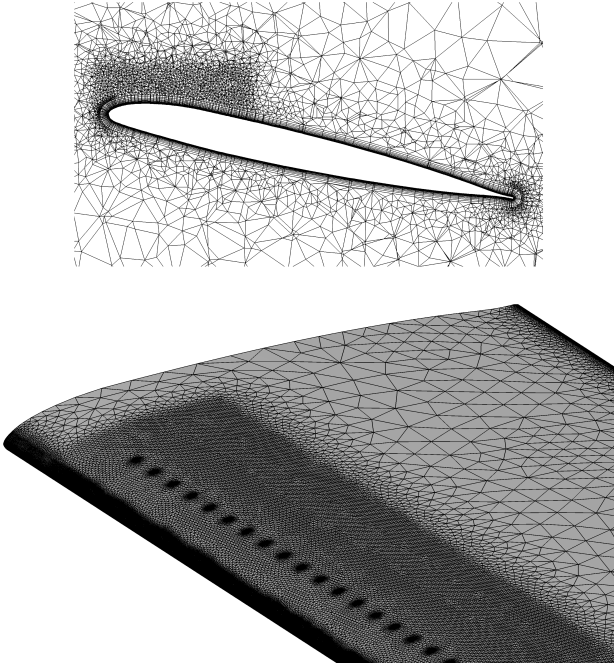


Figure 4: Mesh of air jet simulations.

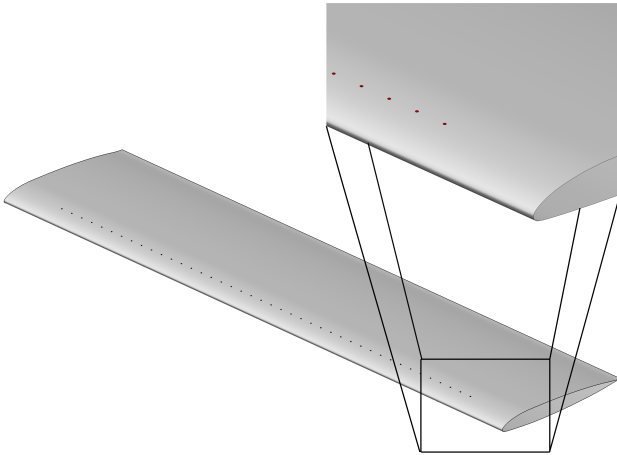


Figure 5: OA209 airfoil with patches

finer by measured values from the experiment (Figure 5). Due to losses in the pipes an effective patch diameter A^* was calculated, based on experimental mass flow measurements using:

$$\dot{m}_{jet} = K \sqrt{\frac{\gamma}{RT_0}} \left(\frac{2}{\gamma+1} \right)^{\frac{\gamma+1}{2\gamma-2}} p_0 A^* \quad (4)$$

where the jet mass flow and jet pressure of the simulations was equal to that of the experimental data. The experimental jet diameter of 3 mm was thus reduced to a patch diameter of 2 mm.

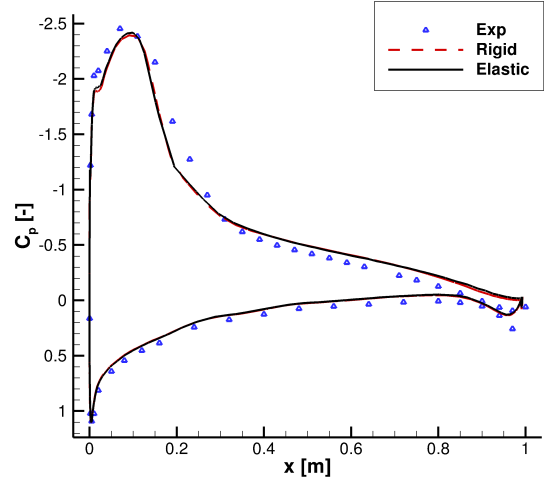


Figure 6: Pressure distribution at $Ma = 0.4, Re = 2.8 \cdot 10^6, \alpha = 6^\circ$

Aeroelastic Equilibrium at Mach 0.4

The effect of fluid-structure coupled aeroelastic simulations on static wind tunnel configurations of the OA209 airfoil was investigated at Mach 0.4 and Reynolds number $2.8 \cdot 10^6$. Figure 6 shows the C_p distribution at the model midpoint with DLR-TAU and PyCSM at $\alpha=6^\circ$ and $C_L = 0.74$. The airfoil shows a broad, subsonic suction peak near the front of the airfoil followed by a monotonic recompression of the flow. The rear loading of the airfoil is low, but there is a discontinuity at around $x/c=0.95$ due to the airfoil tab which is visible in the pressure distribution. The surface C_p distributions in the mid span compare quite well with experimental data, with some slight differences at the downstream end of the suction peak. The pressure distributions of rigid and elastic 3D airfoil simulations are very similar, with the elastic airfoil showing a slightly higher suction peak. The difference between the two numerical cases was $\Delta C_L=0.0097$, which is around the same as the experimental error of $\Delta C_L=0.01$.

During the experiments the displacement of the airfoil model were measured at the midspan position by a PiColor™ system. This marker based optical measurement tool uses Stereo Pattern Recognition (SPR) with two cameras from different directions. For the test conditions in this paper the PiColor™ system measured with an accuracy of ± 0.1 mm. Figure 7 shows lift integrated from the pressure data at the airfoil midline (C_L) as a function of the maximum vertical displacements (h_{max}) at the airfoil midline at four angles of attack for attached flow. Attached flow test cases are chosen as being representative of the aerodynamic loads while retaining relatively simple aerodynamics. It can be seen that around $C_L=0.2$ the simulation overestimates the airfoil deformation, but that with increasing lift the computed vertical displacement matches the experimentally measured dis-

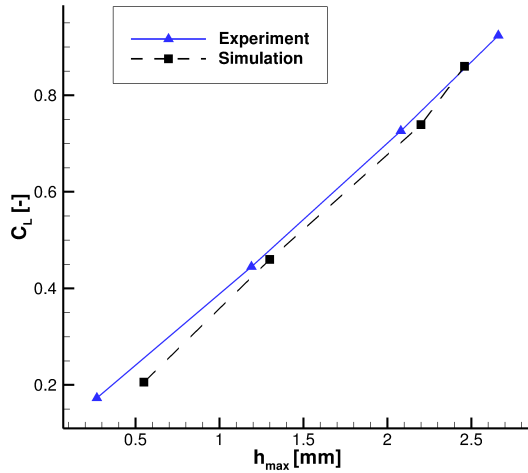


Figure 7: Lift coefficient versus maximum vertical displacement in the mid span

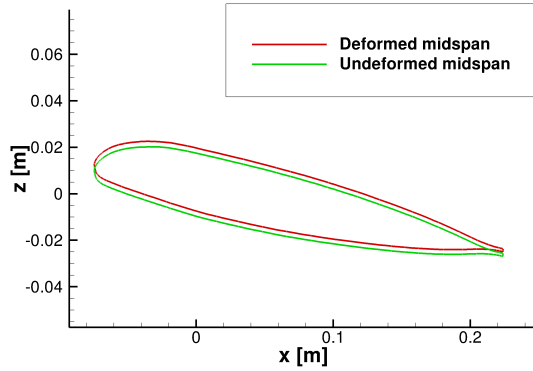


Figure 8: Comparison of undeformed and deformed airfoil midspan at $\alpha = 8^\circ$

placement within the experimental uncertainty.

The computations were performed at the same angles of attack as used in the experiments ($\alpha=2^\circ, 4^\circ, 6^\circ, 8^\circ$) and it can be seen that the computation always slightly overestimates the midsection lift for each angle of attack. At the highest angle of attack, the simulation shows the airfoil at the beginning of stall, whereas the experiment still shows fully attached flow. This slight difference in the static stall angle appears to be an aerodynamic effect of the simulation and not an effect of the coupling, since the airfoil shows no significant rotation under load. Figure 8 shows a comparison of the undeformed and deformed grid midspan at $\alpha = 8^\circ$. The grid slice of the deformed grid shows a constant deflection from leading to trailing edge. The deformed airfoil shows no significant trailing edge deformation or elastic twist.

The aeroelastic steady simulations on the OA209 airfoil at Mach 0.4 have shown that the elastic influence is negligible because of the very stiff structure. This is estimated to also be the case for dynamic pitching cases,

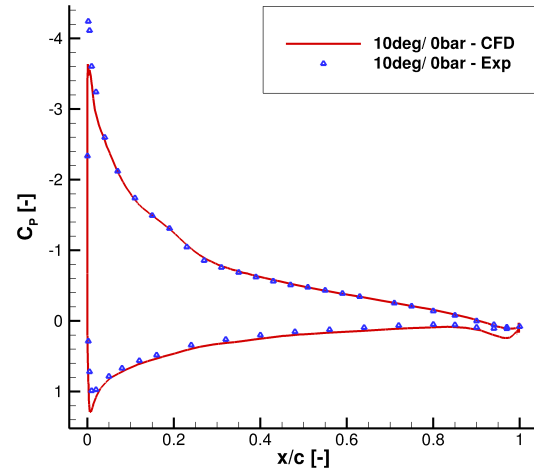


Figure 9: Pressure distribution without blowing at $Ma=0.3, Re=1.16 \cdot 10^6, \alpha=10^\circ$.

but explicit computations for dynamic pitching are still in development. The effect of three-dimensionality was then further investigated for this model without elastic coupling at the reduced loads seen at Mach 0.3.

Mach 0.3 results without air jet blowing

The aerodynamics of the static airfoil in the DNW-TWG was investigated at $Ma=0.3, Re=1.16 \cdot 10^6$. Flow conditions without air jet blowing for $\alpha=10^\circ, 13^\circ$ and 20° were simulated and compared to experimental results. Figure 9 shows the C_p distribution at $Ma = 0.3, Re = 1.16 \cdot 10^6, \alpha = 10^\circ$ without air jet blowing. The suction peak is more localized toward the front of the airfoil than seen at Mach 0.4, but the flow towards the rear of the airfoil is similar. At $\alpha=10^\circ$ the flow is fully attached and there is a good agreement between the experiment and numerical simulations.

Figure 10 shows the experimental and numerical C_p distributions at the model midline without air jet blowing at $\alpha=13^\circ$ ($P_{jet} = 0$ bar). In contrast to the experimental data the numerical result has separated flow, and similar to the results at Mach 0.4, the flow has separated earlier in the simulation than in the experiment. The start of the flow separation strongly depends on the turbulence model, and the Menter SST turbulence model used appears to stall around 1° earlier than the experiment. This is seen by the good agreement in Figure 10 between the separated flow in the CFD at $\alpha=13^\circ$ and the experiment at $\alpha=14^\circ$, where the flow has also separated. Although there is good agreement on the upstream half of the airfoil, the downstream half shows much lower pressures in the experiment than in the CFD, indicating that the separated flow in the experiment is stronger than in the CFD. Interesting to note in this diagram is that the critical pressure for supersonic flow at Mach 0.3, $C_{p_{crit}}=6.94$, is ex-

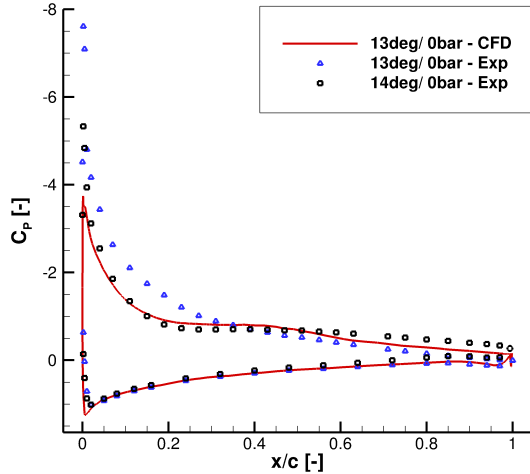


Figure 10: Pressure distribution without blowing at $Ma=0.3$, $Re=1.16 \cdot 10^6$, $\alpha=13^\circ$.

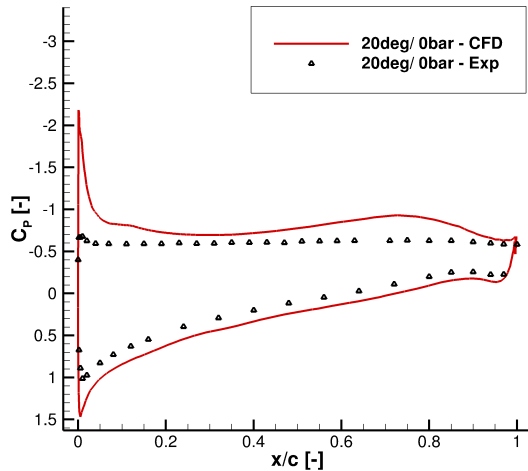


Figure 11: Pressure distribution without blowing at $Ma=0.3$, $Re=1.16 \cdot 10^6$, $\alpha=20^\circ$.

ceeded by the suction peak in the experiment at $\alpha=13^\circ$ at two pressure stations, indicating a localised region of supersonic flow.

Figure 11 shows a comparison of the C_p distribution at $\alpha = 20^\circ$ for numerical and experimental data. The flow here is fully separated in both the experiment and CFD, and no true convergence is achieved in the numerical computations, as expected for RANS computations of fully separated flow. The CFD predicts a sharp suction peak which is not measured during the experiment, and the lift in the CFD is $C_L=1.08$ rather than $C_L=0.7$ as expected in the experiment.

The simulations of attached flow cases without blowing have shown good agreement with experimental data. The CFD results of separated flow at $\alpha=13^\circ$ showed that the separation angle is predicted at a lower angle in CFD

that for the experiment. At $\alpha=20^\circ$ a significantly higher lift is achieved in the simulations than seen in the experiment, probably due to the use of a RANS solver for fully separated flow.

Mach 0.3 results with air jet blowing

Numerical simulations at $Ma=0.3$, $Re=1.16 \cdot 10^6$ investigated the effect of blowing through portholes for flow control at $P_{jet}=3-10$ bar and $\alpha=10^\circ$, 13° and 20° . Figure 12 shows the suction side of the airfoil with the air jet patches. The surface C_p values are shown with colored contours. The absolute air jet pressure of 10bar is directly defined at the surface patches. White volume streamlines are started at the surface of the patches which model the jet inflow, and indicate the movement of the compressed air mass which is ejected from the jets. The flow exits the jets normal to the airfoil chord and causes a blockage in the flow. The jet is quickly turned downstream by the oncoming flow and the jet path diverges slightly from the airfoil contour as the flow progresses downstream and mixes with the freestream flow. The mixture of the streamtraces of the main flow and the air jets is shown in Figure 13. The streamlines in black indicate the material from the freestream.

The freestream flow passes between the jets and is accelerated by the constriction, as seen in the reduced surface pressure between the jets. In the lee behind each jet is a bounded separated region followed by slower moving flow. Gas from this slow-moving region is accelerated with the supersonic flow of the jet, resulting in a region of low pressure. Due to reducing the physical size of the jet patch in the CFD from the physical $\phi=3$ mm to $\phi=2$ mm to match the experimentally measured pressure and mass flux, it is expected that the field away from the jet will be correctly simulated (due to a correct energy balance) but that the flow very near to the jet will not be physically correct.

Figure 15a shows the pressure distribution of a cut plane through the air jet ($\alpha=13^\circ$, $P_{jet}=10$ bar). The plotted streamtraces of the main flow are deflected upward by the air jets, with flow upstream of the jet following the jet upward after the stagnation point and slow flow from the leeward side of the jet being entrained into the jet. The rapid entrainment and mixing of the air jet with the freestream is visible. The interaction of the main flow and the jets is also shown in Figure 14. The skin friction streamtraces show the flow separation behind each air jet. The oncoming flow is influenced within an area of two times the air jet diameter. The flow forms a stagnation point and horseshoe vortex in front of each jet.

Figure 15b shows the pressure distribution of a cut plane between the air jets at the same condition. In contrast to the cut plane at the jet position, the streamlines between the jet are nearly undisturbed, only being moved downward toward the airfoil by the displacement of the jet after the jet position. The usual subsonic suc-

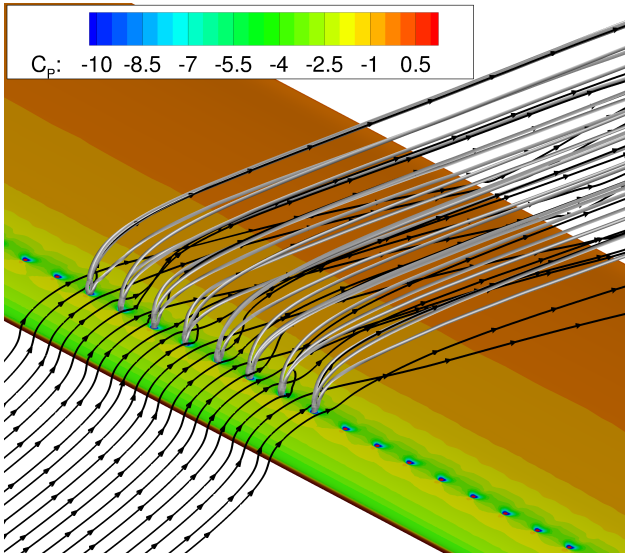


Figure 12: CFD result for the geometry of the jet array at $Ma=0.3$, $Re=1.16 \cdot 10^6$, $\alpha=13^\circ$ and $P_{jet}=10$ bar.

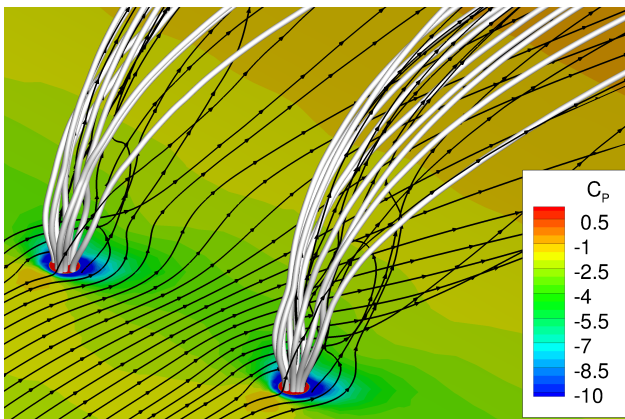


Figure 13: CFD result for the geometry of a single jet from the array at $Ma=0.3$, $Re=1.16 \cdot 10^6$, $\alpha=13^\circ$ and $P_{jet}=10$ bar.

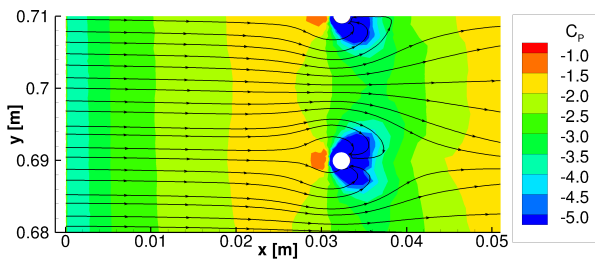


Figure 14: CFD results of the pressure distribution with skin friction streamtraces for $Ma=0.3$, $Re=1.16 \cdot 10^6$, $\alpha=13^\circ$ and $P_{jet}=10$ bar. Flow is from left to right.

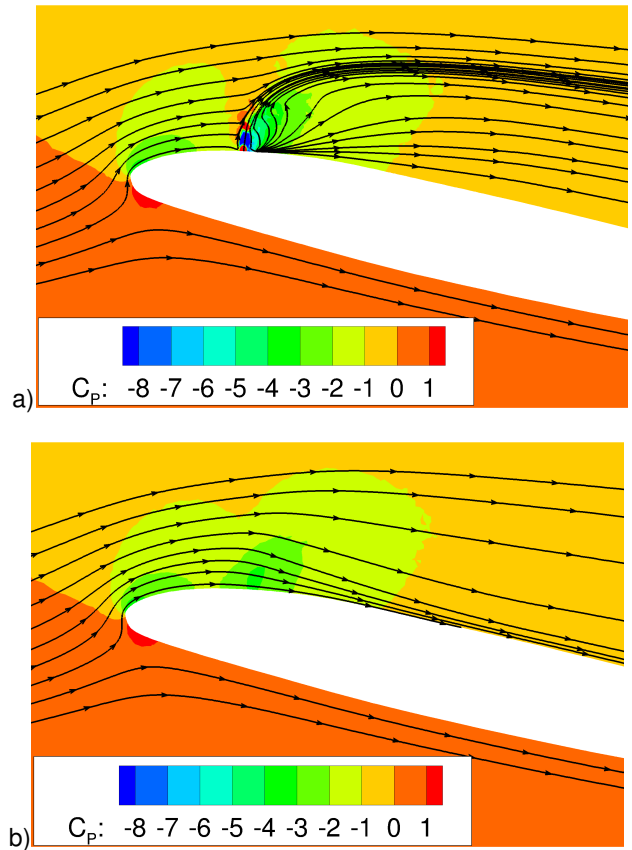


Figure 15: Pressure distribution cut plane at constant y for $Ma=0.3$, $Re=1.16 \cdot 10^6$, $\alpha=13^\circ$ and $P_{jet}=10$ bar for: a) through an air jet b) between two air jets. Flow is from left to right.

tion peak is visible at the leading edge of the airfoil, and this is followed by a second suction peak as the flow is accelerated between the jets.

The pressure distribution at the suction side of the OA209-FCD airfoil with air jet blowing was investigated by pressure-sensitive paint (PSP), as reported further in [20]. The PtTFPP-based PSP was applied with a spray gun directly to the surface of the airfoil and a UV-LED lamp illuminated the paint surface. The pressures could be computed from the fluorescence intensity taken in the "intensity method". The thickness of the paint was 10 ± 2 micrometer.

Figure 16a shows the CFD pressure distribution of air jets on the suction side of the airfoil. The characteristic geometry of the pressure around the air jets is visible as a stagnation point upstream of the jets and a band of lower pressure between the jets as the freestream flow passing between the jets is restricted. Downstream in the lee of each jet is a region of low pressure due to the upward acceleration of the flow with the jet, and this region is very localized in the CFD. The CFD grid is locally around 0.2 mm in this region, which is coarser than the resolution if the PSP data which is projected onto a 1 mm grid in this region. As seen in Figure 16b the PSP data

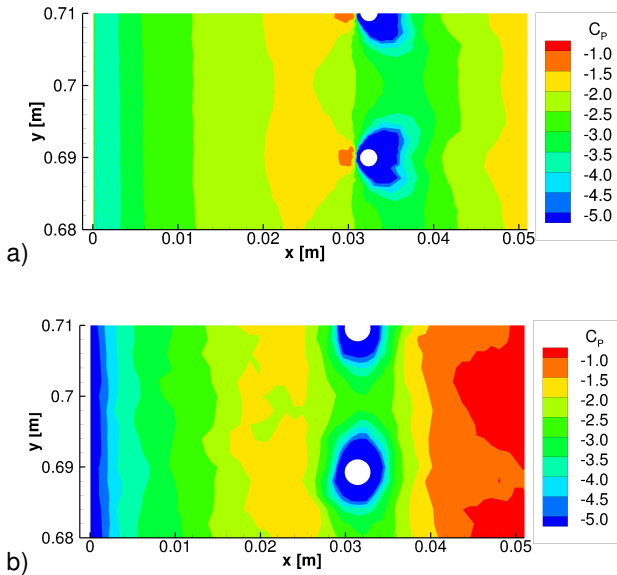


Figure 16: Pressure distributions for $Ma=0.3$, $Re=1.16 \cdot 10^6$, $\alpha=13^\circ$ and $P_{jet}=10$ bar for: a) CFD results with DLR-TAU b) PSP pressure measurements. Flow is from left to right.

shows a similar result to the CFD, but the coarser resolution means that neither the stagnation point upstream of each jet nor the strong suction in the jet lee are resolved. The pressure downstream of the jet compares well between PSP and CFD, and the pressure upstream in the suction peak is qualitatively similar, but quantitatively a little less in the CFD than in the experiment. Starting at 16% chord the PSP measurements show a large pressure variation up to the trailing edge of the profile. A possible explanation of this unexpected effect is a temperature influence of the cold air jet stream on the surface of the model, since the PSP has a temperature sensitivity of -800Pa/K .

As indicated by the PSP measurements, the pressure distributions for $Ma=0.3$, $Re=1.16 \cdot 10^6$, $\alpha=13^\circ$ and $P_{jet}=10$ bar now show attached flow. Figure 17 shows a good agreement between the experiment and numerical result, since in contrast to the cases without blowing, both cases now show attached flow. The suction peak on the front of the airfoil is reduced in height, similar to the reduction noted for the case without blowing, but now a second subsonic suction peak appears between the jets. With the exception of a small separation region behind the jets, the flow both upstream and downstream of the jets remains attached. The flow after the jets is comparable in all cases. Qualitatively, the change between separated flow without blowing and attached flow with blowing is similar for the experiment at $\alpha=14^\circ$ and the CFD at $\alpha=13^\circ$.

At $\alpha=10^\circ$, the effect of jet blowing for fully attached flow can be seen (Figure 18), with the reduction in the suction peak at the front of the airfoil when blowing is used, and the appearance of a second suction peak. The suction peak at the air jets is quite well predicted

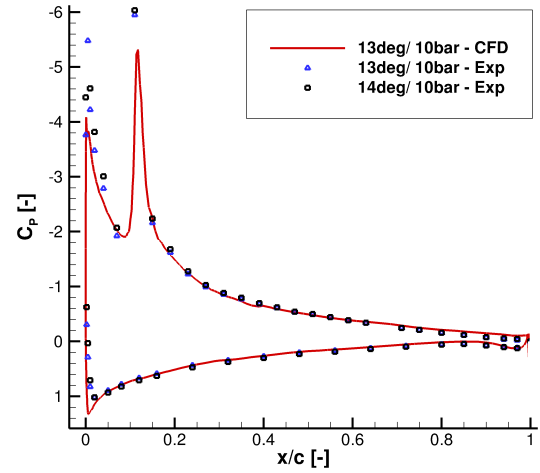


Figure 17: Pressure distribution at $Ma=0.3$, $Re=1.16 \cdot 10^6$, $\alpha=13^\circ$ and $P_{jet}=10$ bar.

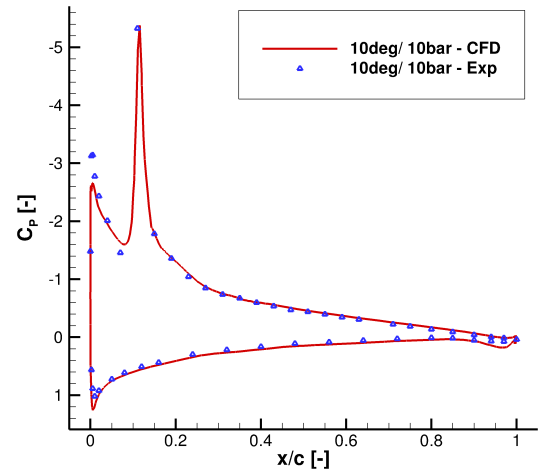


Figure 18: Pressure distribution at $Ma=0.3$, $Re=1.16 \cdot 10^6$, $\alpha=10^\circ$ and $P_{jet}=10$ bar.

by CFD, but the suction peak at the front of the airfoil is narrower for the experiment than in the CFD.

Figure 19 shows the C_p distribution at $\alpha=20^\circ$, and there is a much better agreement between the experiment and numerical data than seen without blowing. In both cases the flow on the back of the airfoil is separated, but the flow of the front of the airfoil is attached. A similar primary suction peak is seen for CFD and experiment, but the suction peak around the air jets is much lower in the experiment. As noted in [20], this can be due to a discretisation problem, since as seen in Figure 16, this sensor is positioned in a region of high pressure gradient and may simply spatially miss the peak.

In general the pressure distributions with blowing are well matched by the CFD, and especially in fully separated flow at $\alpha=20^\circ$, the results are much better with

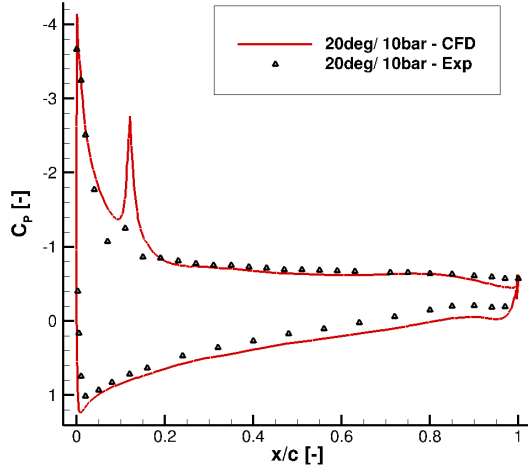


Figure 19: Pressure distribution at $Ma=0.3$, $Re=1.16 \cdot 10^6$, $\alpha=20^\circ$ and $P_{jet}=10$ bar.

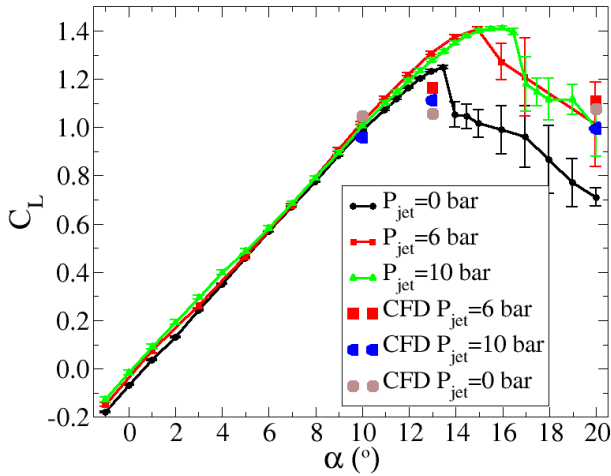


Figure 20: Lift polars with and without constant blowing at $Ma = 0.3$, $Re = 1.16 \cdot 10^6$

blowing than without. When comparing the lift at the center section, C_L is integrated from C_p and then the forces need to be corrected for the momentum force F due to the air jets, computed from the impulse by:

$$F = \dot{m}v = \dot{m}/L_{act} \sqrt{\frac{2\gamma RT_0}{\gamma+1}}. \quad (5)$$

The jet is assumed sonic at the surface of the model, and T_0 , is the total temperature. Further, \dot{m} is the mass flux, $L_{act}=0.84$ m is the breadth of model which is acted upon by the actuation jets, and $\gamma=1.4$ and $R=287$ J/kg/K are the gas constants for dry compressed air.

During the experiment the lift polars at $Ma = 0.3$ with and without constant air jet blowing were measured. (Figure 20). The differences in C_L between $P_{jet} = 0, 6, 10$ bar was investigated and the influence of blowing considered. Without air jet blowing, C_L increases linearly up to $C_L = 1.25$ at $\alpha=13.45^\circ$. The flow then separates and

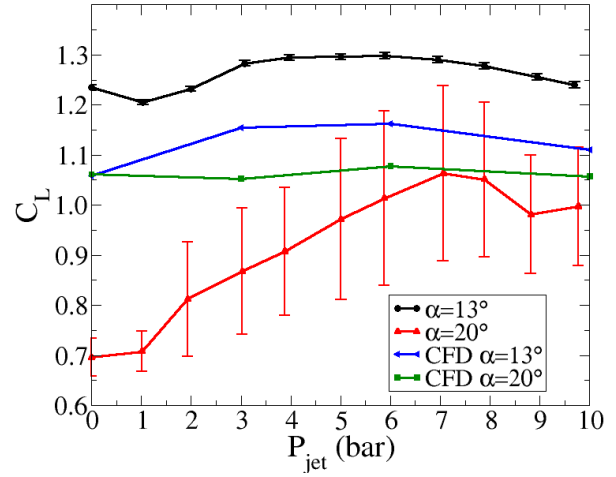


Figure 21: Lift variation with constant blowing pressure at constant angle of attack at $Ma = 0.3$, $Re = 1.16 \cdot 10^6$

the lift decreases up to the maximum angle measured at $\alpha=20^\circ$. With $P_{jet} = 6$ bar air jet blowing, the maximum lift increased to $C_L=1.41$. The same maximum lift was observed for $P_{jet} = 10$ bar. After the maximum C_L the lift decreased almost linearly. Blowing at both $P_{jet} = 10$ bar and $P_{jet} = 6$ bar caused a significant increase in the lift noted at $\alpha=20^\circ$.

In addition to the experimental data, Figure 20 shows the CFD results for simulations with and without air jet blowing. Simulations without air jet blowing were performed at $\alpha=7^\circ, 10^\circ, 13^\circ$ and 20° . The simulation predicted separated flow at $\alpha=13^\circ$ with $C_L=1.06$ which is around $\Delta\alpha=1^\circ$ earlier than seen in the experiment. The data at $\alpha=10^\circ$ is quite similar to experimental results. The lift coefficient, $C_L=1.08$, for the separated flow case without blowing at $\alpha=20^\circ$ is higher than in the experiment. The lift coefficients at $\alpha=20^\circ$ with blowing are well predicted by CFD simulations.

During the experiment the influence of air jet pressure variation was tested for two angles of attack $\alpha=13^\circ$ and 20° . The pressure polars are shown in Figure 21 which includes the variation between $P_{jet}=0-10$ bar. For the experiments, the points illustrate the mean and the scatter bars illustrate the standard deviation of data taken over 10 seconds of measurement. At $\alpha=20^\circ$ in the experiments the C_L minimum is at $P_{jet} = 0$ bar. With increasing air jet blowing the lift increases linearly up to $C_L=1.05$ at $P_{jet}=7$ bar (52% increase). After that the lift decreases with increasing pressure up to $P_{jet}=10$ bar. Experimental data have shown that the flow without air jet blowing was attached at $\alpha = 13^\circ$. With a blowing pressure of 1 bar, the flow separates and C_L decreases. As the air flow pressure increases, C_L increases up to $P_{jet}=5-6$ bar. Constant blowing with $P_{jet}=3-7$ bar improves the aerodynamics for static wind tunnel configurations.

Figure 21 also shows the CFD results for $\alpha=13^\circ$ and 20° with $P_{jet}=0, 3, 6, 10$ bar. The C_L value at $\alpha=13^\circ$ and $P_{jet}=0$ bar shows the separated flow with lower lift than seen in the experimental data. The lift increases with

increasing jet blowing (14.5%) but the offset to the experimental data is almost constant. The maximum lift is predicted for $P_{jet}=3-6$ bar. The CFD simulations at $\alpha=20^\circ$ are quite similar to the experiment, with a similar progression in pressure, but as noted previously the lift at $P_{jet} = 0$ bar is significantly higher than in the experiment (See also Figure 11). With increasing air jet blowing the lift remains almost constant due to the fact that the C_L is overpredicted by CFD simulations.

Conclusion

Numerical investigations on a three-dimensional OA209 airfoil with flow control by air jets are compared with experiments at static conditions. RANS calculations for the DNW-TWG wind tunnel with a 1 m x 1 m adaptive-wall test section setup are performed to investigate the three-dimensional effects of this nominally two-dimensional configuration. Aeroelastic investigations of the midspan displacement, by coupling with a finite-element model of the airfoil at $Ma = 0.4$ and $Re=2.8 \times 10^6$ showed a good agreement in the maximum normal deflection h_{max} for points with attached flow. The computation stalled earlier than the experiments, and this results in a reduction of the aerodynamic force provided at this point, but still a good agreement in the deflection expected for this normal load. A small influence of the airfoil deformation on the aerodynamics can be seen in the numerical results, but the effect is less than the experimental uncertainty, and it could be shown that the airfoil did not have a torsion in addition to the heave.

A numerical investigation of flow control by air jets at the leading edge was presented for multiple static test cases at $Ma = 0.3$ and $Re=1.16 \cdot 10^6$. A variation of air jet pressure and its influence on stall suppression is shown to be in good agreement with experiments except in the case where no flow control is used (blowing pressure of zero), where the airfoil stalled earlier in CFD than in the experiments. The lift in the fully stalled regime were significantly overestimated without blowing. Particularly the reattachment of stalled flow by the application of blowing could be demonstrated at $\alpha=13^\circ$.

An investigation of the flow around the jets showed the stagnation point in front of the jets and a separated region behind the jets. The vertical acceleration of the slow flow behind the jets and the acceleration of the freestream flow between the jets could be observed, and these observations were shown to be in good agreement with experimental pressure distributions from pressure sensitive paint. The comparison of the lift-pressure polars showed qualitatively good results for the CFD with the exception of the lift prediction at $\alpha=20^\circ$ where no blowing was used.

References

- [1] Gardner, A.D., Richter K., Mai, H. and Neuhaus, D., *Experimental investigation of air jets for the control of compressible dynamic stall*, Journal of the American Helicopter Society, Vol. 58, No. 4, 2013. DOI: 10.4050/JAHS.58.042001
- [2] Gardner, A.D., Richter, K., and Rosemann, H., *Numerical investigation of air jets for dynamic stall control on the OA209 airfoil*, CEAS Aeronautical Journal, Vol. 1, No. 1, 2011. DOI: 10.1007/s13272-011-0002-z
- [3] Packard, N.O., Thake, M.P. Jr., Bonilla, C.H., Gompertz, K., and Bons, J.P., "Active control of flow separation on a laminar airfoil," *AIAA Journal*, Vol. 51, (5), 2013, pp. 1032–1041. doi: 10.2514/1.J051556
- [4] Prince, S.A., Khodagolian V., and Singh, C., "Aerodynamic stall suppression on airfoil sections using passive air-jet vortex generators," *AIAA Journal*, Vol. 47, No. 9, pp. 2232-2242, 2009. DOI: 10.2514/1.41986
- [5] Singh, C., Peake, D.J., Kokkalis, A., Coton, F.N. and Galbraith, R.A., "Control of rotorcraft retreating blade stall using air-jet vortex generators," 29th European Rotorcraft Forum, Friedrichshafen, Germany, 16-18 September 2003.
- [6] Singh, C., Peake, D.J., Kokkalis, A., Khodagolian, V., Coton, F.N. and Galbraith, R.A., "Control of Rotorcraft Retreating Blade Stall Using Air-Jet Vortex Generators," *Journal of Aircraft*, Vol. 43, (4), 2006, pp. 1169–1176. doi: 10.2514/1.18333.
- [7] Mai, H., Dietz, G., Geissler, W., Richter, K., Bosbach, J., Richard, H., and de Groot, K., "Dynamic stall control by leading edge vortex generators," *Journal of the American Helicopter Society*, Vol. 53, No.1, 2008, pp. 26-36. DOI: 10.4050/JAHS.53.26
- [8] Heine, B., Mulleners, K., Joubert, G., Raffel, M., "Dynamic stall control by passive disturbance generators," *AIAA Journal*, Vol. 51, No.9, 2013, pp. 2086-2097. DOI: 10.2514/1.J051525
- [9] Rehman, A., Kontis, K., "Synthetic jet control effectiveness on stationary and pitching airfoils", *Journal of Aircraft*, Vol. 43 No. 6, pp. 1782-1789, 2006. DOI: 10.2514/1.20333
- [10] Richter, K., Le Pape, A., Knopp, T., Costes, M., Gleize, V., Gardner, A.D., *Improved two-dimensional dynamic stall prediction with structured and hybrid numerical methods*, Journal of the American Helicopter Society, Vol. 56, No. 4, 2011. DOI 10.4050/JAHS.56.042007.

COPYRIGHT STATEMENT

The author(s) confirm that they, and/or their company or organisation, hold copyright on all of the original material included in this paper. The authors also confirm that they have obtained permission, from the copyright holder of any third party material included in this paper, to publish it as part of their paper. The author(s) confirm that they give permission, or have obtained permission from the copyright holder of this paper, for the publication and distribution of this paper as part of the ERF2014 proceedings or as individual offprints from the proceedings and for inclusion in a freely accessible web-based repository.

- [11] Klein, A., Lutz, Th., Kramer, E., Richter, K., Gardner, A.D. and Altmikus, A.R.M., "Numerical comparison of dynamic stall for two-dimensional airfoils and an airfoil model in the DNW-TWG", *Journal of the American Helicopter Society*, Vol. 57, No. 4, 2012, DOI: 10.4050/JAHS.57.042007
- [12] Stickan, B., Dillinger, J., *Steady and unsteady simulation of aerostabil windtunnel experiments*, IFASD - 15th International Forum on Aeroelasticity and Structural Dynamics, June, Paris, 2011.
- [13] Mai, H., Neumann, J., Hennings, H., *Gust Response: A Validation Experiment And Preliminary Numerical Simulations*, IFASD - 15th International Forum on Aeroelasticity and Structural Dynamics, June, Paris, 2011.
- [14] Hassan, D., Ritter, M. *Assesment of the ONERA/DLR numerical aeroelastics prediction capabilities on the HIRENASD configuration*, IFASD-2011-109, Paris, 2011.
- [15] Schwamborn, D., Gardner, A.D., von Geyr, H., Krumbein, A., Lüdeke, H., Stürmer, A., *Development of the TAU-Code for aerospace applications*, 50th International Conference on Aerospace Science and Technology, Bangalore, India, June 26-28, 2008.
- [16] Menter, F.R., *Zonal Two Equation $k - \omega$ Turbulence Models for Aerodynamic Flows*, AIAA 93-2906, 23rd AIAA Fluid Dynamics, Plasmadynamics and Lasers Conference, Orlando, FL, July 6-9, 1993. DOI: 10.2514/6.1993-2906
- [17] Beckert, A., Wendland, H., *Multivariate Interpolation for Fluid Structure Interaction Problems using Radial Basis Function*, Aerospace Science and Technology Vol. 5, February, 2001.
- [18] Voss, G., Cumnuantip, S., Neumann, J., *A Steady Aeroelastic Analysis of an Unmanned Combat Aircraft Vehicle Conceptual Design*, 29th AIAA applied Aerodynamic conference, Honolulu. Hawaii, 27-30 June, 2011. DOI: 10.2514/6.2011-3020
- [19] Gardner, A.D., Richter, K., "Effect of the model-sidewall connection for a static airfoil experiment", *Journal of Aircraft*, Vol. 50, No. 2, pp. 677-680, March-April 2013.
DOI: 10.2514/1.C03201
- [20] Gardner, A. D., Klein, C., Sachs, W., Henne, U. , Mai, H., Richter, K., "Investigation of three-dimensional dynamic stall on an airfoil using fast response pressure sensitive paint", American Helicopter Society 70th Annual Forum, Montreal, Quebec, May 20-22, 2014.